PAPER

Experimental and modeling study of ZnO:Ni nanoparticles for near-infrared light emitting diodes

Imen Elhamdi, [ID] *[a] Hajer Souissi,[a] Olfa Taktak,[a] Jaber Elghoul,[bc] Souha Kammoun,[a] Essebti Dhahri [ID] [a] and Benilde F. O. Costa[d]

This work is devoted to the synthesis and study of the different properties of ZnO nanoparticles (NPs) doped with the Ni element. We have used a simple co-precipitation technique for the synthesis of our samples and various structural, morphological and optical techniques for their analysis. Energy-Dispersive X-ray spectroscopy (EDX) confirms the stoichiometry of the samples. The X-Ray Diffraction (XRD) patterns reveal the hexagonal wurtzite phase of polycrystalline ZnO with a $P63mc$ space group. Debye Scherrer and Williamson–Hall methods show that the average size of crystallites is around 40 nm. Transmission electron microscopy (TEM) images confirm the XRD results. The optical spectrum of $Zn_{0.95}Ni_{0.5}O$ shows the presence of near-band-edge (NBE) ultraviolet emission. The absorption defect bands appearing near the blue–green region and near infrared emission are attributed to the Ni^{2+} intra-3d luminescence. The electronic structure of the Ni^{2+} doped ZnO NPs confirms the T_d site symmetry of Ni^{2+} in the ZnO host crystal and leads to a perfect correlation between calculated and experimental energy levels.

1 Introduction

ZnO is an attractive wide band gap II–VI semiconductor for potential applications in photonics, electronics, biosensors, biomedicine and spintronics.[1–10] Due to good properties such as wide band gap (3.37 eV) and high excitation binding energy (60 meV), ZnO is among the useful materials for applications such as nanodevice fabrication, gas sensors, light emitting diodes, dye-sensitized solar cells, light emitting devices, thin film transistors, and optoelectronic devices.[10–18] Likewise, it is widely used in various medicinal, cosmetic, and food products. Due to the anti-microbial and anti-tumor activities, ZnO is included in some cosmetic lotions as it is also known to maintain UV blocking and absorbing capabilities.[5] ZnO can also be used as an astringent for wound healing, hemorrhoid treatment, eczema treatment and excoriation treatment in human medicine and veterinary science. ZnO nanoparticles (NPs) have also antibacterial, anti-neoplastic and antimicrobial properties.[5] In order to modify the structure of the electronic band and improve its applications in various

semiconductor spintronic devices, ZnO has been doped with different transition metals (TM).[6–18] The Zn^{2+} in the crystal lattice structure of ZnO will be replaced by metal ions from doping, thus increasing the number of free electrons. This improves the electronic properties of the oxide semiconductor. ZnO NPs have been prepared by simple, low cost, solution-based methods, such as chemical precipitation, sol–gel synthesis, solvothermal and hydrothermal methods.[16–21] The co-precipitation method is among the methods that have been widely used for the synthesis of NPs. It is considered to be promising method due to the ease of control of the particle size and the need for low temperatures in the synthesis process.

In the present work, the ZnO NPs doped with Nickel were synthesized by using chemical co-precipitation method. The structural, morphological and optical properties of the ZnO NPs doped with Ni^{2+} were studied. We present a detailed crystal field analysis of electron energy levels of Ni^{2+} doped ZnO NPs. A theoretical study, based on the Racah tensor algebra methods, was performed for the Ni^{2+} center ($3d^8$) with T_d site symmetry.

[a]Laboratoire de Physique Appliquée, Groupe de Physique des Matériaux Luminescents, Faculté des Sciences, Université de Sfax, BP 1171, 3000 Sfax, Tunisia. E-mail: imen85356@gmail.com

[b]Imam Mohammad Ibn Saud Islamic University (IMSIU), College of Sciences, Department of Physics, Riyadh 11623, Saudi Arabia

[c]Laboratory of Physics of Materials and Nanomaterials Applied at Environment (LaPhyMNE), Faculty of Sciences in Gabes, Gabes University, 6072 Gabes, Tunisia

[d]University of Coimbra, CFisUC, Physics Department, P-3004-516 Coimbra, Portugal

2 Experimental methods

2.1 Materials

The precursors used to prepare $ZnO:Ni^{2+}$ nanopowders, purchased from Sigma Aldrich, consist of high purity chemicals without further purification which are: zinc sulfate heptahydrate $ZnSO_4 \cdot 7H_2O$ (ACS reagent, 99%), nickel chloride

hexahydrate $NiCl_2 \cdot 6H_2O$ (99.9%, trace metals basis), sodium hydroxide NaOH (reagent grade, $\geq$98%) and ethanol C_2H_5OH.

2.2 Synthesis of Ni-doped ZnO NPs

As it is known, the co-precipitation process does not require expensive and complex equipment and it is robust and reliable to control the shape and size of the particles.[18] Therefore, we used this process to synthesize the Ni doped ZnO nanoparticles. The process consists of dissolving 5 g of zinc sulfate heptahydrate and 0.105 g of nickel chloride in 300 ml of ultra-pure water. Then, 50 ml of NaOH (10 M) was added dropwise to the solution which was stirred magnetically for 2 h at room temperature to produce a white gelatinous precipitate. Then we filtered and washed the white precipitates using ethanol and ultrapure water several times. This step was followed by drying for 4 h at 200 °C in a furnace and grinding in an agate mortar. Finally, the nanoparticles obtained were heat treated at 500 °C in air atmosphere for 2 h.

2.3 Characterization techniques

The crystal structure of the Ni doped ZnO NPs was analyzed on the basis of powder X-ray diffraction (XRD) data. The powder diffraction patterns were recorded with a STOE STADI P powder diffractometer in Debye–Scherrer geometry using Ge(111) monochromatic Cu-Kα1-radiation of wavelength $\lambda = 1.5406$ Å. The XRD measurements at room temperature were carried out in the locked coupled mode in the 2θ range from 10° to 80° with a step width of 0.02°. The surface morphology, size distribution and the composition of the elements of Ni-doped ZnO NPs were realized with Transmission Electron Microscopy TEM made on a JEOL 2011 JEOL JEM 2000 Ex microscope operating at accelerating voltage of 100 kV and probe current of $\sim$800 pA coupled to an Energy-Dispersive X-ray analysis (EDX) device. The micrograph patterns were recorded at 80 kV and the selected area electron diffraction (SAED) pattern was recorded by keeping camera constant 100 cm. The Fourier Transform Infrared (FTIR) was used to identify the elemental constituents of the material. The FTIR spectrum was recorded at room temperature in the range of 4000–400 cm^{-1} using Thermo Nicolet 380 with KBr pellet technique. An integrating sphere compatible with the powder samples attached to the UV-Vis-IR spectrophotometer (Shimadzu UV-3101 PC) has been used to measure of the optical absorbance in the wavelength range from 300 to 1800 nm. Room temperature photoluminescence (PL) spectra of our NPs have been carried using a JobinYvon-Horiba Triax 190 spectrometer with a 488 nm line of an argon ion laser and a spectral resolution of 0.3 nm, coupled with a liquid nitrogen-cooled CCD detector.

3 Theoretical crystal-field study

When the free transition ion Ni^{2+} is used as a dopant of ZnO NPs, the energy levels are subdivided. The group theory allows us to predict the subdivision of the energy levels just by specifying the symmetry of the site occupied by the transition ion. This theory determines the number and the degeneracy of these energy levels and the value of these energies will be determined

only by numerical calculation. The transition ion Ni^{2+} with 3d^8 electronic configuration occupies a T_d site symmetry in ZnO. The decomposition of the $D^{(L)}$ reducible representations of the SO(3) group (rotation group of the free transition ion) into irreducible representations of the site group T_d leads to the stark levels of the Ni^{2+} ions in the ZnO host matrix. Fig. 1 represents the splitting of the Ni^{2+} (3d^8) energy level under the crystal field with T_d site symmetry. The energies of the stark levels (without and with the spin–orbit interaction) are obtained only by numerical calculation when using the Racah method. In order to study the energy levels splitting of Ni^{2+}, we diagonalize the 45 × 45 matrix associated to the following Hamiltonian:[15–17,22–27]

$$H = H_0 + H_{ee}(B,C) + H_{Trees}(\alpha) + H_{CF}(D_q) + H_{SO}(\zeta) \quad (1)$$

H_0 is the Hamiltonian configuration associated to the energy E_0 which is 45 times degenerated. H_{ee} is associated to the electron–electron repulsions which leads to the Russell-Saunders terms: ^{4}F (ground state according to Hund rule), ^{4}P, ^{2}H, ^{2}G, ^{2}F, ^{2}D, ^{2}D$'$ and ^{2}P excited terms. The analytical eigenvalues of H_{ee} are a function of the Racah parameters B and C.[15] The Trees correction Hamiltonian H_{Trees} represents the two-body orbit–orbit polarization interaction. The analytical eigenvalues of H_{Trees} are function of the Trees parameter α.[15–18,22] For tetrahedral symmetry T_d and following the Wybourne's notation, the crystal field Hamiltonian H_{CF} is given by:[15–18,22–28]

$$H_{CF}(T_d) = 21D_q \left[C_0^{(4)} + \sqrt{\frac{5}{14}} \left(C_4^{(4)} + C_{-4}^{(4)} \right) \right] \quad (2)$$

D_q is the crystal field strength parameter. H_{CF} is a function of the Racah tensor operators $C_q^{(k)}$, with:[15–18,22–28]

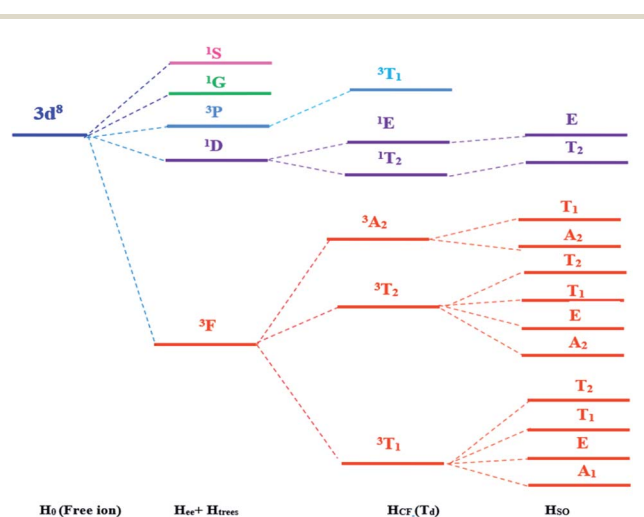$$C_q^{(k)} = \sqrt{\frac{4\pi}{(2l+1)}} Y_k^q \quad (3)$$

Fig. 1 Energy levels of the Ni^{2+} ion (3d^8) under the crystal field with T_d symmetry and spin orbit coupling.

Y_k^q are the spherical harmonics.

Using the Racah tensor algebraic methods and as we know that HCF is of the intermediate strength,[28] we have calculated numerically the matrix elements of $C_q^{(k)}$ in the basis functions $\{|d^N L S M_L M_S\rangle\}^{15-18,22-28}$

$$\langle LSM_LM_S|C_q^{(k)}|L'SM_{L'}M_S\rangle = (-1)^{L-M_L}\begin{pmatrix} L & k & L' \\ -M_L & q & M_{L'} \end{pmatrix}$$
$$\times \langle LS\|C^k\|L'S\rangle \tag{4}$$

$\begin{pmatrix} L & k & L' \\ -M_L & q & M_{L'} \end{pmatrix}$ is the 3j-symbols and $\langle LS\|C^k\|L'S\rangle$ is the reduced matrix elements.

The B, C, and D_q parameters are deduced from the optical spectra. The eigenvalue of the spin–orbit coupling Hamiltonian H_{SO} depends on ξ parameter.

The free ion Ni^{2+} parameters are: $B_0 = 1041$ cm^{-1}, $C_0 = 4831$ cm^{-1}, $\alpha_0 = 42$ cm^{-1} and $\zeta_0 = 702$ cm^{-1}.[16,17,22,29-31]

An approximation is used between the parameters of doped and the free Ni^{2+} ion:[26,27]

$$B = N^4 B_0,\ C = N^4 C_0,\ \alpha = N^4\alpha_0\ \text{and}\ \zeta = N^2\zeta_0 \tag{5}$$

The average reduction factor N is defined as:[26,27]

$$N^2 = \frac{1}{2}\left(\sqrt{\frac{B}{B_0}} + \sqrt{\frac{C}{C_0}}\right) \tag{6}$$

We created a Maple software code to determine the electronic structure of a transition ion having 3d^n electronic configurations and occupying a site with symmetry determined by one of the 32-point crystallographic groups. The ref. 26 and 27 provide more information about this code. This code produces the same results as Yeung and Rudowicz's code.[32]

4 Results and discussion

4.1 Energy-dispersive X-ray spectroscopy analysis (EDX)

The EDX spectrum of the prepared ZnO NPs doped with Ni^{2+} is shown in Fig. 2. We know that peak C in the EDX spectrum is linked to the emission of the carbon ribbon used during the measurement. We note the presence of Zn and O as main components with low levels of Ni. This confirms the correct insertion of the doping element during preparation. In addition, there is no trace of peaks of external impurities in the studied compound confirming the purity of this material. The observation of low intensity peak for nickel doped ZnO in Fig. 2, confirms the proper incorporation of nickel Ni^{2+} in the ZnO structure. The quantitative analysis of the compositional elements presents in Ni-doped ZnO NPs using EDX spectra is presented in Table 1. From this analysis, the average Ni/Zn atomic percentage ratio is derived to be 5.01% in Ni-doped
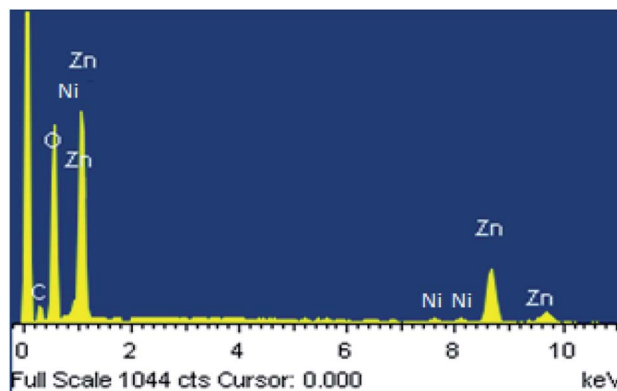

Fig. 2 EDX spectrum of Ni doped ZnO NPs.

Table 1 The quantitative analysis of the compositional elements presents in Ni-doped ZnO NPs using EDX

Spectrum for Zn$_{0.95}$Ni$_{0.05}$O	O	Ni	Zn
Weight (%)	39.08	2.75	58.17
Ni/Zn ratio		0.0472	
Atomic (%)	72.42	1.31	26.27
Ni/Zn ratio		0.0498	

ZnO samples. This result confirms the good agreement with the experimental concentration used during the synthesis.

4.2 XRD diffraction

The XRD pattern of Fig. 3 clearly shows a good crystallinity of prepared samples Zn$_{0.95}$Ni$_{0.05}$O NPs. The XRD peaks, located at 2θ values of 31.786° (100), 34.4256° (002), 36.2574° (101), 47.5444° (102), 56.5858° (110), 62.8694° (103), 66.3757° (200), 67.9516° (112) and 69.0743° (201), have been indexed using the standard ICDD file No. 36-1451 for ZnO.[33] This XRD analysis confirms the single phase with a hexagonal wurtzite structure of ZnO lattice (space group $P6_{3mc}$). It is noted that the wurtzite structure is not affected by the Ni transition ion doping. The Zn$_{0.95}$Ni$_{0.05}$O diffraction peaks show a small shift towards
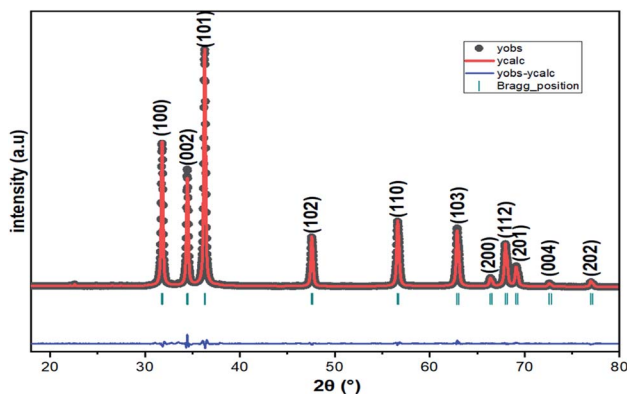

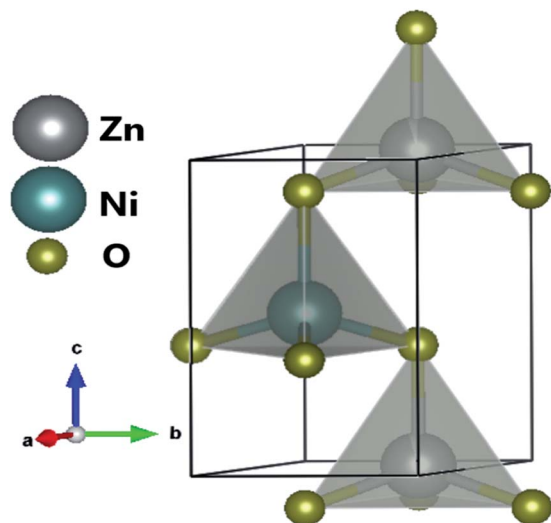Fig. 3 Powder X-ray diffraction pattern of Zn$_{0.95}$Ni$_{0.05}$O NPs.

    © 2022 The Author(s). Published by the Royal Society of Chemistry

Fig. 4 Crystal structure of ZnO doped with Ni^{2+}.

higher 2θ angle values compared to undoped ZnO NPs. In addition, the intensity of these peaks has decreased and the line widths broadened for the $Zn_{0.95}Ni_{0.05}O$ NPs compared to the undoped ZnO NPs. The increase in lattice disorder and the deformation induced by the Ni^{2+} substitution can explain the change in XRD pattern. The ZnO diffraction peak (101) is the most intense peak indicating that the crystallographic preferential orientation is according to (101). In this structure, the Ni^{2+} ion replaces the Zn^{2+} ion, by substitution, in the ZnO structure and occupies a tetrahedral Td site symmetrically surrounded by four oxygen atoms with a slight distortion (Fig. 4).[11,12]

Interplanar distance between the planes of given Miller indices h, k and l called d_{hkl} as a function of the lattice constants (a, c) is given by the following relation:[19,20]

$$\frac{1}{d_{hkl}^2} = \frac{4}{3}\frac{(h^2 + hk + k^2)}{a^2} + \frac{l^2}{c^2} \tag{7}$$

The plane spacing d_{hkl} satisfies the Bragg's law:[9]

$$n\lambda = 2d_{hkl}\sin\theta \tag{8}$$

Table 2   Results with Fullprof refinement

R_p		R_{wp}		R_{exp}	χ^2
4.75		6.13		2.49	6.05

a (Å)	b (Å)	c (Å)	α (°)	β (°)	γ (°)
3.249_7	3.2497	5.2057	90.0000	90.0000	120.0000

Atom	X	Y	Z		Occupation
Zn	0.3333	0.6667	0.0000		0.9254
Ni	0.3333	0.6667	0.0000		0.0254
O	0.3333	0.6667	0.3833		1.0010

N is the order of diffraction (usually $n = 1$), λ is the X-ray wavelength.

The lattice parameters a, b and c for $Zn_{0.95}Ni_{0.05}O$ NPs are calculated from eqn (1) and (2) ($a = b = 3.2497$ Å and $c = 5.2086$ Å). The lattice parameters for undoped hexagonal wurtzite ZnO are $a = b = 3.2513$ Å and $c = 5.2092$ Å.[21] The XRD refinements were also performed by Rietveld refinement software (Fullprof). The calculated pattern is consistent with the observed data and gives the same results for the lattice parameters a, b and c (Fig. 2). The refined crystallographic parameters are given in Table 2. The values of the parameters a and c of the $Zn_{0.95}Ni_{0.05}O$ NPs are smaller compared to those of the undoped ZnO NPs, which is related to the fact that the ionic rays of the dopant Ni^{+2} (0.69 Å) is lower than the ionic radii of the substituted Zn^{+2} (0.74 Å). The value of interplanar spacing d_{101}(2.4760 Å) for $Zn_{0.95}Ni_{0.05}O$ calculated from XRD data for (101) plan shows a slightly decrease compared to d_{101} (2.4770 Å) for undoped ZnO. This behavior is surely due to the variation in bond lengths and angles between atoms caused by the distortion of the NiO_4 tetrahedron, causing lattice stress. The tensile stress causes the peak to shift to lower 2θ values due to the increased spacing d, whereas the compressive stress plays an opposite role.

In the direction of c axis, the Zn–O bond length L has been calculated using the following formula:[19,20]

$$L = \sqrt{\frac{a^2}{3} + \left(\frac{1}{2} - u\right)^2 c^2} \tag{9}$$

The positional parameter u in the wurtzite structure measures the amount which each atom gets displaced with respect to the next.[33,34] The parameter u is determined by the relation:

$$u = \frac{1}{3}\left(\frac{a}{c}\right)^2 + \frac{1}{4} \tag{10}$$

The value of u is of 0.375 when the network is ideal. The variation of u indicates a modification of the lattice parameters. The calculated L is of 1.9779 for $Zn_{0.95}Ni_{0.05}O$ (L is of 1.9787 for undoped ZnO). A good agreement between L of this study and with those reported in literature[21] is obtained which supports the results of the present study.

The volume of the unit cell for the hexagonal system has been calculated using the following relation:[19]

$$V = \sqrt{3}\Big/2a^2c = 0.866a^2c \tag{11}$$

The volume of the unit cell is of 47.6349 Å^3.

4.2.1 Debye–Scherrer method. The crystallite size D of $Zn_{0.95}Ni_{0.05}O$ nanoparticles was calculated from the Debye–Scherrer's formula from XRD pattern. This formula is given by the following expression:[35]

$$D = \frac{0.89\lambda}{\beta\cos\theta} \tag{12}$$

The incident X-ray radiation wavelength λ is of 0.15418 nm. The Bragg angle θ represents the position of the diffraction peak

in the diffractograms. β is expressed in radian and represents the full width at half maxima (FWHM) of X-ray diffraction peak. The crystallite size D is calculated from the intense XRD peak and was found to be 36.06 nm.

The density of dislocation (δ) measures the defects concentration in nanostructures. The δ is considered as the ratio of the dislocation length and volume of the crystal and is calculated using the equation:[36]

$$\delta = 1/D^2 \qquad (13)$$

The crystallite size D is calculated above from eqn (6). The calculated value of dislocation density (δ) for synthesized $Zn_{0.95}Ni_{0.05}O$ is of 7.6870×10^{-4} nm^{-2}.

4.2.2 Williamson–Hall method. The broadening of the DRX peaks arises not only from the crystallites size effect, but also from the stress in the particles. The Williamson–Hall method makes it possible to calculate the size of the crystallites D and also the value of the micro deformation ε. The eqn (8) represents the Williamson–Hall model modified, which manifests the Uniform Deformation Model (UDM):[37]

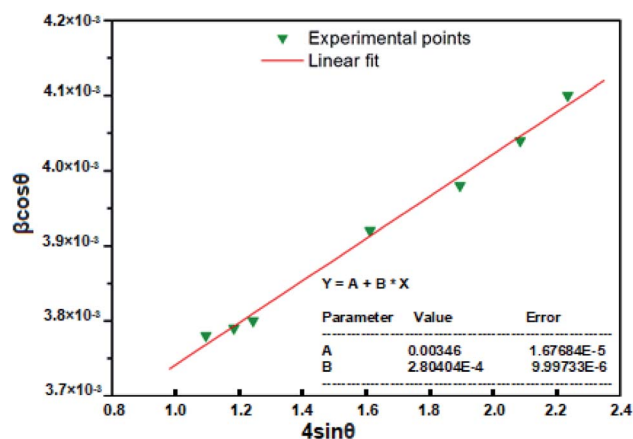$$\beta \cos \theta = 0.89\lambda/D + 4\varepsilon \sin \theta \qquad (14)$$

Fig. 5 The W–H analysis of $Zn_{0.95}Ni_{0.05}O$ assuming UDM model.

λ is the wavelength of incident X-ray radiation, β is expressed in radian and represents the full width at half maxima (FWHM) of the peaks of X-ray patterns.

By using Origin 2018, we have plotted ($\beta \cos \theta$) as a function of ($4 \sin \theta$) for the preferred orientation peaks in the XRD pattern (following peaks (100), (002), (101), (102), (110), (103) and (112)) of $Zn_{0.95}Ni_{0.05}O$ NPs with the wurtzite hexagonal phase. From the obtained Williamson–Hall plots (Fig. 5), the crystallite size and the strain deduced from the intersection y-axis and slope of the linear fit was 39.6 nm and 2.8040×10^{-4}, respectively. The crystallite size evaluated by the Williamson–Hall model is larger than that obtained by the Scherrer model. This is due to the fact that the effect of broadening of the X-ray peaks of Fig. 3, results from the size of the crystallites and the presence of deformation, and this latter is completely neglected in the Scherrer method. The strain ε obtained from the Williamson–Hall model is an important factor to consider and has a remarkable effect on the size of the crystallites.

4.3 Transmission electron microscope (TEM) studies

The TEM observations are is a good tool for the morphological studies of ZnO NPs and to determine the particle size and shape. TEM micrographs of $Zn_{0.95}Ni_{0.05}O$ NPs, presented in Fig. 6a and b, indicate the formation of nanometric particles with a well-confined but agglomerated structure. When compared to undoped ZnO, the nickel doped ZnO samples have a random hexagonal and spherical shape with lower particle sizes. The distribution of particles is heterogeneous and the particles appear to be broadly agglomerated. Because of the increased surface to volume ratio, which results in an increase in attractive force, the particles tend to agglomerate together. This is due to nickel incorporation in the ZnO lattice. The Fig. 7 shows the particle size distribution histogram of $Zn_{0.95}Ni_{0.05}O$ NPs. The particle size spans from 20 to 100 nm on the histogram, with an average size of 40.173 nm. This average value is equivalent to the estimated crystallite size calculated by Williamson–Hall method. The SAED image of $Zn_{0.95}Ni_{0.05}O$ system, shown in Fig. 8, reveals a ring pattern confirming the polycrystalline structure of the sample. The indexing of SAED pattern matches well with XRD data.
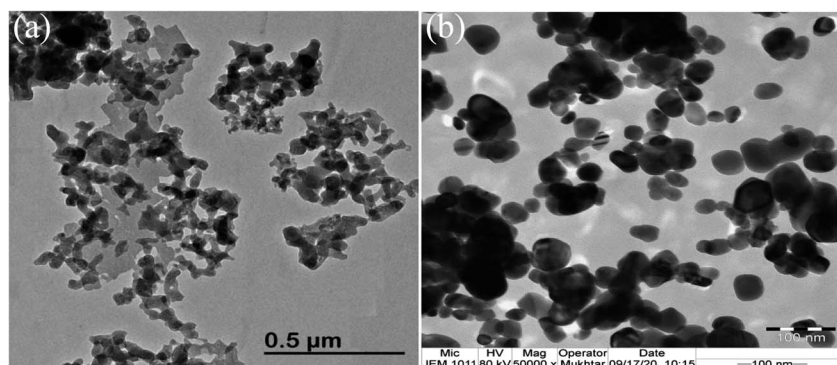

Fig. 6 TEM image of Ni doped ZnO NPs (a) around 500 nm and (b) around 100 nm.
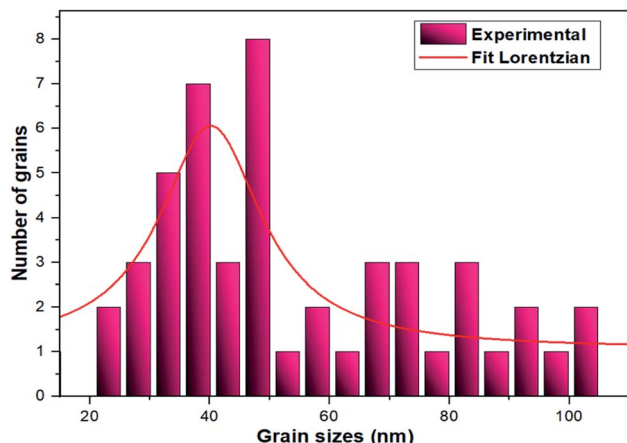
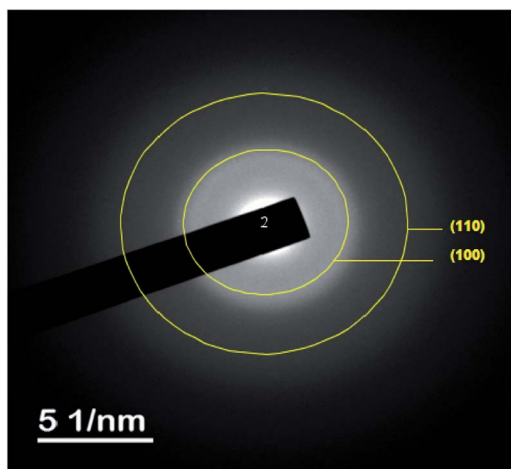Fig. 7 Histogram of grain size distribution of Ni-doped ZnO NPs.

Fig. 8 The selected area electron diffraction (SAED) image Ni doped ZnO NPs.

4.4 Fourier transform infrared (FTIR) studies

The FTIR spectrum for $Zn_{0.95}Ni_{0.05}$ NPs was recorded in the range of 400–4000 cm^{-1} and is shown in Fig. 9. The FTIR spectrum provides further information on functional groups. The presence and the position of the absorption bands depend on the crystal structure, chemical composition and particle morphology. FTIR measurements confirmed the creation of the wurtzite structure in Ni doped ZnO. Table 3 lists the persistent IR frequencies, as well as the vibrational assignments, that are responsible for Ni-doping in ZnO at room temperature. In the hexagonal wurtzite type crystal structure, FTIR spectra reveal the existence of characteristic peaks in the ranges of 450 to 650 cm^{-1}, which correspond to Zn–O stretching vibrational modes.[38] The change in bond lengths of Zn–O lattice when Ni ion replaces Zn ion leads to a shift of the vibration frequency of Zn–O to a frequency higher than 434 cm^{-1} corresponding to undoped ZnO. This confirms the incorporation of Ni^{2+} ions as a substitute of Zn^{2+} ions in ZnO structure. The vibrations of ZnO–Ni local bonds and defect states are responsible for the
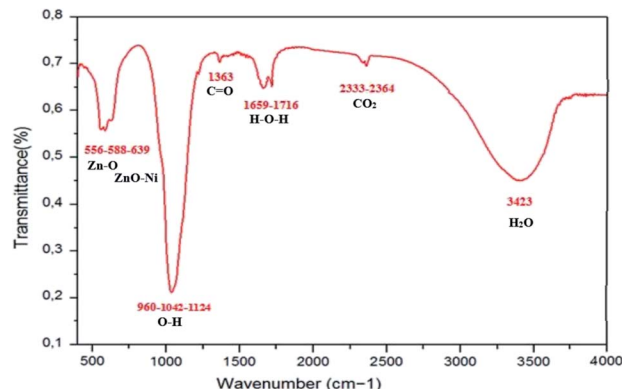

Fig. 9 FTIR spectra of Ni-doped ZnO NPs at room temperature.

Table 3 FTIR results for ZnO doped with Ni

Assignments	Wavenumber (cm^{-1})
Zn–O stretching mode	450–650
Vibrations of ZnO–Ni local bonds	640
Defect states	960
O–H asymmetric stretching	1042
Symmetric stretching of the carboxyl group (C=O)	1350–1400
H–O–H bending vibration	1659
CO_2 molecule in air	2320–2400
O–H stretching vibration of H_2O	3443

absorption bands that emerge about 640 and 960 cm^{-1}, respectively.[38] From literature, these frequency are absent in undoped ZnO sample. The bands around 1042 cm^{-1} are strong with asymmetric stretching of resonance interaction between vibration modes of oxide ions in the nanocrystals. The asymmetric and symmetric stretching of the carboxyl group (C=O) correlate to the absorption peaks seen at 1350 and 1400 cm^{-1}. The peak around 1659 cm^{-1} in ZnO is ascribed to H–O–H bending vibration and is assigned to a little amount of H_2O in the ZnO NPs. The absorption peaks observed in the range 2320–2400 cm^{-1} are due to the existence of CO_2 molecule in air. The broad absorption peak (2700–3500 cm^{-1}) centered at 3443 cm^{-1} is ascribed to normal polymeric O–H stretching vibration of H_2O molecule in Zn–O lattice.[38] The appearance of these bands in manufactured nanoparticles could be attributed to atmospheric water content adsorption.

4.5 Investigation of the optical spectra

The UV-Visible optical absorption spectrum of $Zn_{0.95}Ni_{0.05}O$ NPs recorded at room temperature (300–1800 nm) and the PL spectrum (800–1300 nm) are illustrated in Fig. 10.

4.5.1 The optical band gap E_g. The optical band gap E_g of $Zn_{0.95}Ni_{0.05}O$ semiconductor was calculated using the Tauc's law given by:[39–41]

$$\alpha h\nu = A(h\nu - E_g)^n \qquad (15)$$
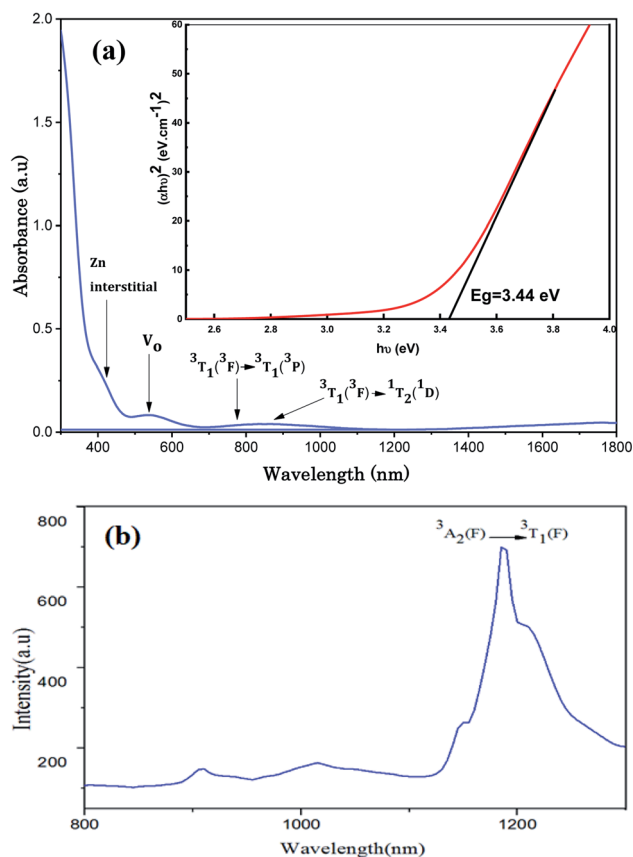
Fig. 10 (a) Absorption spectrum (300–1800 nm) and (b) PL spectrum (800–1300 nm).

where $h\nu$ is the energy of the incident photon, α is the absorption co-efficient and A is a constant. The type of transition depends on the exponent n which can take two values depending on whether the transition is allowed direct ($n = 1/2$) or indirect band gaps ($n = 2$). From Fig. 10a, the optical transition is direct and the energy band gap E_g of $Zn_{0.95}Ni_{0.05}O$ is of 3.44 eV. The value of E_g indicates that the NPs $Zn_{0.95}Ni_{0.05}O$ are characterized by a wide band-gap material useful in optoelectronic devices. We remark that the values of the E_g of the $Zn_{0.95}Ni_{0.05}O$ NPs semiconductors decrease compared to bulk ZnO for which the E_g is 3.37 eV.[16,17]

4.5.2 defects in ZnO. Several recent works have contributed to the search for intrinsic point defects in ZnO nanocrystals.[42–48] Shankari Nadupalli et al. uses electron paramagnetic resonance (EPR) and photoluminescence (PL) spectroscopy to analyze the intrinsic defect structure of ZnO. They compare the findings to previous computational work. The defects are analyzed primarily by considering the microscopic defect structure of the lattice. Intrinsic defects in ZnO modify its electrical and optical properties. Shankari Nadupalli et al. briefly reviews the existing information on the local structure surrounding the defects.[42]

Defects commonly mentioned in ZnO-based nanostructures are:[42–48]

- Oxygen vacancies with different charged states (the +2 charged state (V_O^{2+}), the +1 charged state (V_O^+) and the neutral

state (V_O^0)); the resulting emissions related to this type of defect usually occur near blue–green (approximately 420–550 nm).

- Zn vacancies; the resulting emissions related to this type of defect usually occur near yellow (approximately 550–610 nm).

- Zn interstitials; in the wurtzite ZnO structure, Zn_i occupies the tetrahedral or the octahedral site. When compared to the interstitial occupying tetrahedral site, the octahedral occupancy of Zn_i is shown to be a stable and favorable state.[17] It has been demonstrated that The Co^{2+} implantation generates a high concentration of additional zinc interstitials as it substitutes the Zn ions.[17] This confirms that the intense donor bound exciton emission at 3.36 eV at low temperatures assigned to the D°X line is related to zinc interstitials Zn_i.[17] We assume in this work the same behavior with the incorporation of the transition ion Ni^{2+}. The resulting emissions related to this type of defect usually occur near orange-red (approximately 610–750 nm).

The absorption peak at 430 nm may be due to the electron transition from the valence band to Zn interstitial energy level. The absorption in the green region (511–600 nm) is related to deep level absorption (DLE). VO related defects and V_{Zn} contribute to this broad band absorption. The most common defects in ZnO are oxygen vacancies and generally act as radiative centers in luminescence processes. These oxygen vacancies are considered among the intrinsic defects of n-type ZnO. By capturing electrons they generate a new level of energy that can form ionized vacancies which act as deep defect donors. These deep defects further influence the optical properties of ZnO. The green absorption located at 534 nm is certainly related to the oxygen vacancies.

Electron paramagnetic resonance (EPR) spectroscopy is one approach for properly observing and distinguishing defects in ZnO crystals.[42,46,48] According to Shankari Nadupalli et al., two EPR signals are observed for ZnO nanocrystals at $g = 1.9620$ and $g = 2.0048$, depending on the size and shape of the ZnO particle. These findings suggest that the surface/volume ratio has an impact on the sort of defects incorporated in ZnO. By using the core–shell model, core defects are assigned to EPR lines at $g = 1.9620$, whereas surface/shell defects are attributed to EPR lines at $g = 2.0048$ (Fig. 11). The EPR signal of surface/shell defects is
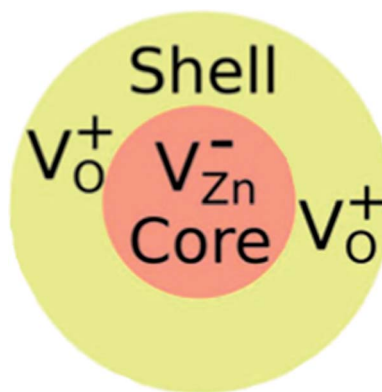

Fig. 11 The surface/shell defects is attributed to an unpaired electron-trapped oxygen vacancy (V_O) site and the core defects is attributed to V_{Zn}^- centers [Shankari Nadupalli].

attributed to an unpaired electron-trapped oxygen vacancy (V_O) site and can either be V_O^+ or V_O^0, depending on the size and morphology of ZnO. Whereas, the EPR signal of the core defects is attributed to V_{Zn}^- defect centers[42] (Fig. 11). This result is specifically for ZnO nanocrystals. According to this concept and by tuning the size of the ZnO nanocrystal, one can achieve a negatively charged (n-type) core with a positively charged (p-type) surface or an exclusive p-type ZnO quantum dot. The core–shell model is only applicable to nanosized ZnO particles and cannot be used to simulate microcrystalline (>500 nm) or bulk ZnO samples.[42,46,48] The research presented by Shankari Nadupalli *et al.* predicted that changing the size of the nanocrystal can change the concentration of intrinsic defects and their location.[42] The size of the nanocrystal and the post-annealing treatments can also affect the UV, green, orange, and red emissions.[42] From ref. 42, the calculated energy level for Zn_i is 0.22 eV below the conduction band and V_{Zn} is 0.30 eV above the valence band. The transition $Zn_i \rightarrow V_{Zn}$ leads to a radiative emission of 2.98 eV (415 nm). The defect level of V_O is located at 0.9 eV above the valence band. Then, the transition between $Zn_i \rightarrow V_O$ results in a radiative emission of 2.38 eV (520 nm).[42]

4.5.3 The determination of crystal field D_q, Racah B, C, Trees α and spin–orbit parameters from absorption spectra.
The optical spectrum of $Zn_{0.95}Ni_{0.05}O$ NPs in the visible region (Fig. 10a and b) show three bands located at:

- 763 nm (13106 cm^{-1}) on the absorption spectrum corresponding to the spin allowed transition $^3T_1$ (^3F) $\rightarrow$ $^3T_1$ (^3P).

- 859 nm (11641 cm^{-1}) on the absorption spectrum corresponding to the spin forbidden transition $^3T_1$ (^3F) $\rightarrow$ $^1T_2$ (^1D).

- 1187 nm (8424 cm^{-1}) on the emission spectrum corresponding to the spin allowed transition $^3A_2$ (^3F) $\rightarrow$ $^3T_1$ (^3F).

The analytical expressions of the Ni^{2+} energies are obtained by calculating the eigenvalues of the Hamiltonian (45 × 45) of eqn (1). The obtained eigenvalues are a function of the average reduction factor N and the crystal field strength D_q. These two parameters have been determined from the observed energies of the absorbance spectra of $Zn_{0.95}Ni_{0.05}O$ NPs recorded at room temperature. We consider the ratio $C/B = 4.64$ of the free ion. The B, C, α and ξ_d parameters are calculated from eqn (5). All the parameters N, D_q, B, C, α and ξ_d are listed in Table 4. The calculated parameters lead to the theoretical energy levels of ZnO NPs doped with Ni^{2+} with the use of the code developed by S. Kammoun *et al.* (Table 5). The reports: $\beta_B = B/B_0 = 0.71$ and $\beta_C = C/C_0 = 0.71$ make clear the covalency effects. The Tanabe–Sugano diagram, schematized in Fig. 12 for Ni^{2+} ion ($C/B = 4.64$), indicates the suitable value for ($Dq/B = 0.57$) by the vertical line obtained from this theoretical analysis.

4.5.4 Photoluminescence (PL) studies.
The photoluminescence PL spectra of $Zn_{0.95}Ni_{0.5}O$ represent the ultraviolet (UV) near-band-edge emission (3.15–3.43 eV) (Fig. 13). On the high-energy side of the PL spectra, the shoulder at 3.3795 eV

Table 4 The parameters values of D_q, N, B, C, α and ξ_d (in cm^{-1}) for Ni^{2+}:ZnO of this work and comparison with literature

Materials/parameters	D_q	N^2	B	C	α	ξ_d
ZnO:Ni^{2+} nanoparticles [this work]	420	0.851	740	3433	30.458	597.8
Ni^{2+} in ZnO[35]	405		795	—		
Zn_2SiO_4:Ni^{2+} (ref. 36)	450		780	3630		

Table 5 Experimental and calculated energies (cm^{-1}) of Ni^{2+} occupying a T_d symmetry in ZnO NPs

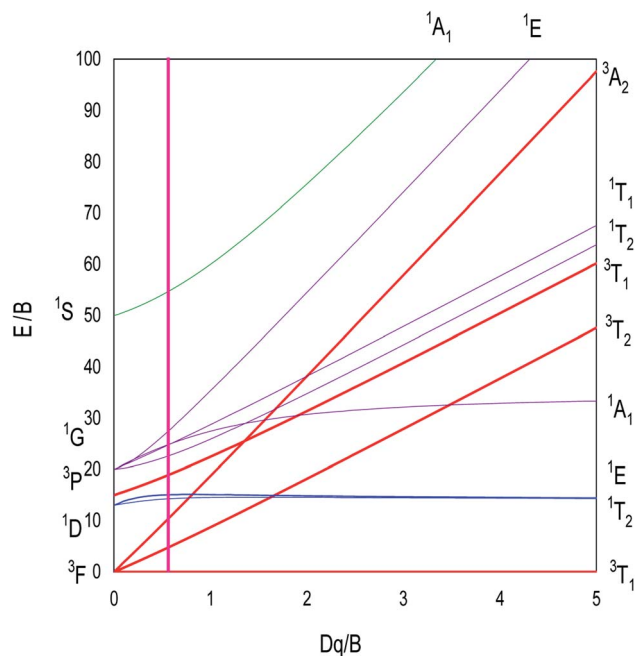| T_d	$E_{observed}$ (cm^{-1})	$E_{calculated}$ (cm^{-1}) T_d site symmetry	T'_d	$E'_{calculated}$ (cm^{-1})
$^3T_1(^3F)$	0	0	A_1	0 (1)
			T_2	140 (3)
			T_1	1002 (3)
			E	1535 (2)
$^3T_2(^3F)$		3564	A_2	3933 (1)
			T_1	4008 (3)
			E	4478 (2)
			T_2	4606 (3)
$^3A_2(^3F)$	8424	7764	T_1	8592 (3)
$^1T_2(^1D)$	11641	11527 (3)	T_2	
$^1E(^1D)$		12111 (2)	$^1A_1$	
$^3T_1(^3P)$	13106	14028	A_1	13824 (1)
			T_2	14110 (3)
			T_1	14685 (3)
			E	14686 (2)
$^1T_1(^1G)$		17712 (3)		
$^1T_2(^1G)$		19310 (3)	T_2	
$^1A_1(^1G)$		19432 (1)	E	
$^1E(^1G)$		21328 (2)	T_1	
$^1A_1(^1S)$		43752 (1)	A_1	

Fig. 12 Tanabe–Sugano diagram for tetrahedral coordinated Ni^{2+} ion with $C/B = 4.64$. The vertical line with $D_q/B = 0.57$ represents the case of $ZnO:Ni^{2+}$ NPs.
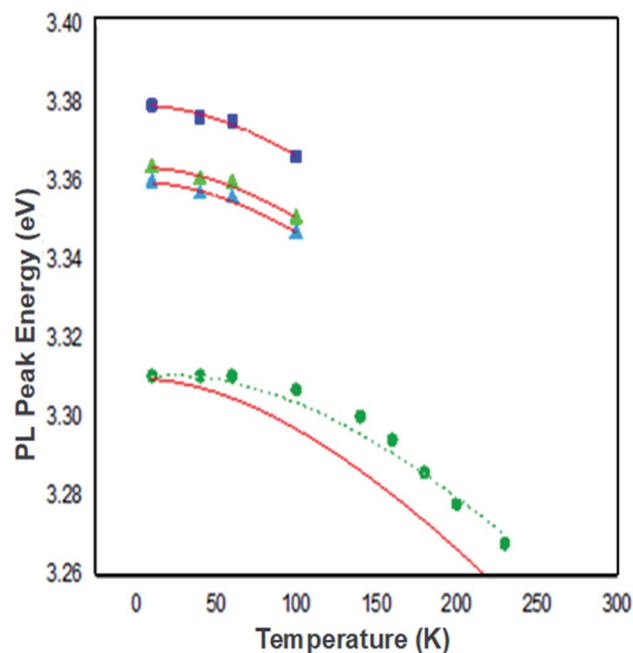

Fig. 14 The temperature dependence of the peak energies for the FX_A emission (solid squares), the $D°X$ emission (solid triangles), BF emission (reverse solid triangles) and the BF-1LO emission (solid circles). Solid lines are calculated using Varshni's formula. The dotted line is calculated using the formula $h\nu = E_g - E_D + k_B T$.

appears at 10 K and is present for all temperatures. With increasing temperature, the shoulder's position moves to the low-energy side and is maintained until around 230 K. This shoulder is attributed to radiative recombination of free excitons FX_A. The recombination at 3.3637 and 3.3599 eV dominate the NBE emissions region at low temperature 10 K. The intensity of these recombinations decrease rapidly with increasing temperature, their position shifts slightly towards low energy and vanishes around 100 K. These modifications characterize the neutral donor-bound exciton $D°X$. In Fig. 14 we plot the curve of the observed energies of FX_A and of $D°X$ as a function of the temperature. We assume that the peak positions of the two emissions FXA and $D°X$ vary with temperature as for the energy

band gap. Then, we have fit the energy temperature dependence curve with the Varshni's semi empirical formula:[17,49]

$$E(T) = E(0) - \frac{\alpha T^2}{T + \beta} \tag{16}$$

From Fig. 14, the Varshni curve is well compatible with the experimental values for the lines FX_A and $D°X$ lines. The fitting parameters for FX_A and $D°X$ lines are respectively:
$\alpha = 7.1382 \ 10^{-4}$ eV K^{-1}, $\beta = 455$ K and $E(0) = 3.3795$ eV and 3.3637 and 3.3599 eV.

The shallow zinc donor state involved in tetrahedral and octahedral interstitial sites proves the existence of two recombinations attributed to the neutral donor-bound exciton $D°X$ (3.3637 and 3.3599 eV).

From the adjustment of the FX_A emission, we can conclude that the shift of this emission with increasing temperature can be due to the shrinking of the forbidden band induced by the temperature. The recombination of both FX_A and $D°X$ at low temperatures is possible in the inter band excitonic transition.[50,51] The thermal activation energy, with increasing the temperature ($T > 60$ K), is enough to a significant amount of $D°X$ ionize into $FX_A(D°X \rightarrow D° + FX_A)$. Due to its high binding energy of 60 meV, FX_A will remain up to room temperature. The $D°X$ emission is no longer visible in the PL spectrum. The emission spectra exhibited a prominent fluorescence peak at 368 nm in visible region due intrinsic and extrinsic defects. An excitonic line, labeled as the surface excitons (SX) for ZnO, is detected between the FXA and $D°X$
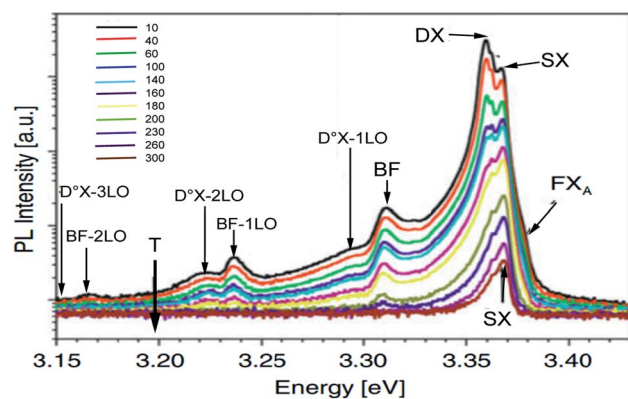

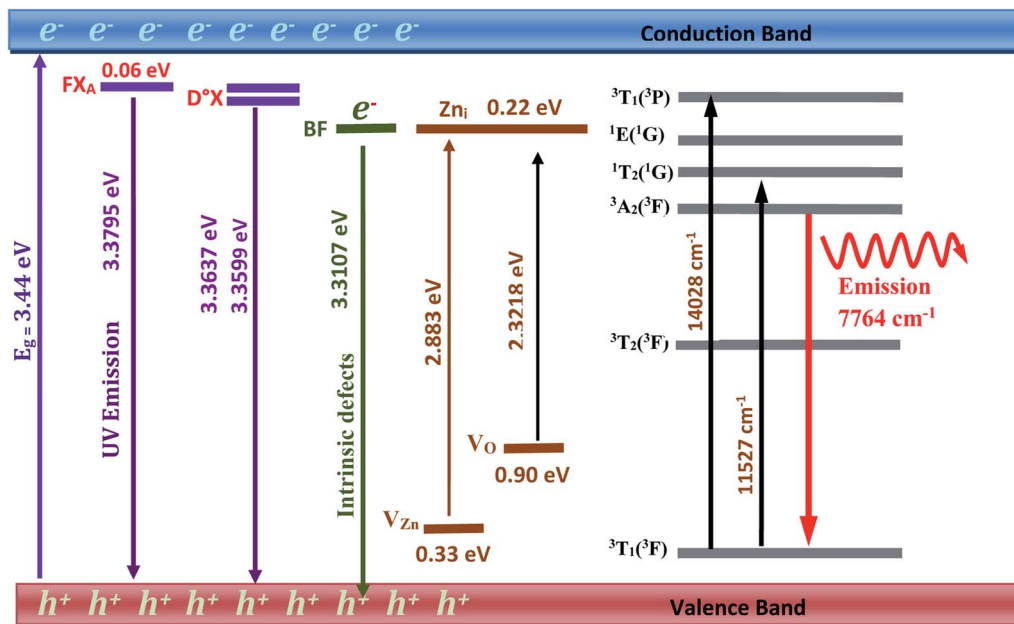Fig. 13 The PL spectra of Ni doped ZnO NPs at temperatures between 10 and 300 K.

© 2022 The Author(s). Published by the Royal Society of Chemistry

Fig. 15   UV-Vis-near infrared energy level diagram of ZnO:Ni^{2+} NPs.

lines at 3.3676 eV. The SX line's intensity is found to be lower than its nanoscale counter-part, which has been related to surface-volume ratio effects. The line positioned at 3.3107 eV at 10 K is maintained up to room temperature and becomes dominant at 300 K, where it is located at 3.2645 eV. This line has the same characteristics as the BF emission line reported in Co^{2+} doped ZnO NPs at 3.314 eV at 15 K and in Co^{2+} doped ZnO NPs at 3.3187 eV at low temperature 10 K, according to comparison.

The recombination of defect-bound carriers with free carriers in some bands is assigned to this line. The experimental data of the BF peak position at various temperatures fit well to the curve (dotted line in Fig. 14) calculated using the formula describing the peak position of emission due to transitions from a donor to the valence band:[52]

$$hv = E_g - E_D + k_B T \qquad (17)$$

E_g denotes the band-gap energy, E_D is the donor's binding energy, T denotes temperature, and k_B denotes the Boltzmann constant. According to Varshni's model, the position peak of the BF emission fluctuates slower with temperature than the energy band gap, as illustrated in Fig. 14.

At 10 K in Fig. 13, several additional peaks appear on the low energy side. These peaks are assigned to the longitudinal optical phonon replica (LO) of the donor bound excitons D°X and BF emission. This interpretation is based on the average spacing of 72 meV.

The peaks at 3.2922, 3.2211, and 3.1536 eV are thought to be D°X (D°X-1LO, D°X-2LO, and D°X-3LO) phonon replicas, the peaks at 3.2360 and 3.1662 eV are thought to be BF phonon replicas (BF-1LO and BF-2LO). Fig. 15 shows all the optical transitions demonstrated in this work.

5   Conclusion

Ni-doped ZnO NPs were successfully prepared by co-precipitation method. The structural and morphological properties of the synthesized nanoparticles have been studied using several techniques. EDX and XRD show a good crystallinity of prepared samples and the incorporation of Ni^{2+} in ZnO structure. It confirms a single phase with a hexagonal wurtzite structure of ZnO lattice (space group $P6_3mc$). The crystallite size determined by the Williamson–Hall model is bigger than that obtained by the Scherrer model. The results of the Williamson–Hall model are more precise because the constraint ε is taken into account and the data is fitted according to this method. The grain size obtained from TEM is equivalent with crystallite size calculated by Willamson–Hall method. From TEM, the morphology of the ZnO:Ni NPs shows a hexagonal structure of spherical shape with smaller grain size compared to undoped ZnO. The SAED ring pattern suggests that the ZnO NPs phase was polycrystalline in structure, and the distance between crystalline planes was consistent with the standard pattern for a wurtzite ZnO crystal structure. FTIR spectra revealed the existence of all functional groups, and this study proved that Ni^{2+} is occupying the Zn^{2+} position. From the UV photo-luminescence spectra, we interpret the ZnO near-band-edge NBE ultraviolet emission. The good fit with Varshni's semi empirical formula of the peak positions *versus* temperature confirms the two near-band-edge NBE ultraviolet emission: the free exciton FX$_A$ and the donor bound exciton emission D°X. The observed values of the BF peak position at various temperatures fit well to the curve calculated using the formula describing the peak location of emission owing to transitions from a donor to the valence band. The blue–green absorption in

ZnO NPs could be owing to an electron transition from the valence band to the Zn interstitial energy level, which is caused by defects. Another absorption in the green region is related to deep level absorption (DLE). It consists with the oxygen vacancies V_O. From the theoretical crystal-field analysis and the visible region, the electronic structure of the Ni^{2+} doped zinc oxide nanoparticles is determined. The T_d site symmetry of Ni^{2+} in ZnO host crystal is confirmed in this theoretical work, which leads to excellent correlations between observed and computed energy levels. According to this study, Ni doping enhances the optical properties of ZnO nanoparticles. In addition to the ultraviolet near-band transitions and the visible blue–green transition, the incorporation of Ni^{2+} in ZnO semiconductor with a high gap leads to the near-infrared emission at 1187 nm which is attributed to intra-3d–3d transition $^3A_2(^3F) \rightarrow {}^3T_1(^3F)$. The d–d transitions of Ni^{2+} are located in the large gap of ZnO nanoparticles. For this reason, $ZnO:Ni^{2+}$ can be used for optoelectronic devices such as near-infrared light-emitting diodes (N-IR LEDs). Moreover, Ni^{2+} doping increases the ZnO matrix defects, which increases the luminescence of the blue–green region.

Conflicts of interest

There are no conflicts of interest to declare.

Acknowledgements

References

1 P. Sheng, L. Yao, P. Yang, D. Yang, C. Lu, K. Cao and W. Li, The origin of enhanced photoelectrochemical activity in metal-ion-doped ZnO/CdS quantum dots, *J. Alloys Compd.*, 2020, **822**, 153700, DOI: **10.1016/j.jallcom.2020.153700**.

2 A. T. Le, M. Ahmadipour and S.-Y. Pung, A review on ZnO-based piezoelectric nanogenerators: Synthesis, characterization techniques, performance enhancement and applications, *J. Alloys Compd.*, 2020, **844**, 156172, DOI: **10.1016/j.jallcom.2020.156172**.

3 F. Z. Bedia, A. Bedia, N. Maloufi, M. Aillerie, F. Genty and B. Benyoucef, Effect of tin doping on optical properties of nanostructured ZnO thin films grown by spray pyrolysis technique, *J. Alloys Compd.*, 2014, **616**, 312–318, DOI: **10.1016/j.jallcom.2014.07.086**.

4 S. Agarwal, L. K. Jangir, K. S. Rathore, M. Kumar and K. Awasthi, Morphology-dependent structural and optical properties of ZnO nanostructures, *Appl. Phys. A*, 2019, **125**, 553. **https://link.springer.com/article/10.1007/s00339-019-2852-x**.

5 Y. Zhang, T. R. Nayak, H. Hong and W. Cai, Biomedical Applications of Zinc Oxide Nanomaterials, *Curr. Mol. Med.*, 2013, **13**(10), 1633–1645.

6 K. Raja, P. S. Ramesh and D. Geetha, Synthesis, Structural and optical properties of ZnO and Ni-doped ZnO hexagonal nanorods by Co-precipitation method, *Spectrochim. Acta, Part A*, 2014, **120**, 19–24, DOI: **10.1016/j.saa.2013.09.103**.

7 J. El Ghoul, Synthesis, structural and optical properties of nanoparticles (Al, V) co-doped zinc oxide, *Bull. Mater. Sci.*, 2016, **39**, 7–12. **https://link.springer.com/article/10.1007%2Fs12034-015-1139-x**.

8 J. El Ghoul, M. Kraini and L. El Mir, Synthesis of Co-doped ZnO nanoparticles by sol–gel method and its characterization, *J. Mater. Sci.: Mater. Electron.*, 2015, **26**, 2555–2562, DOI: **10.1007/s10854-015-2722-z**.

9 J. El Ghoul, Synthesis of vanadium doped ZnO nanoparticles by sol–gel method and its characterization, *J. Mater. Sci.: Mater. Electron.*, 2016, **27**, 2159–2165, DOI: **10.1007/s10854-015-4006-z**.

10 K. Kumar, M. Chitkara, I. S. Sandhu, D. Mehta and S. Kumar, Photocatalytic, Optical and Magnetic properties of Fe-doped ZnO nanoparticles prepared by chemical route, *J. Alloys Compd.*, 2014, **588**, 681–689, DOI: **10.1016/j.jallcom.2013.11.127**.

11 N. Hasuike, K. Nishio, H. Katoh, A. Suzuki, T. Isshiki, K. Kisoda and H. Harima, Structural and electronic properties of ZnO polycrystals doped with Co, *J. Phys.: Condens. Matter*, 2009, **21**, 064215, DOI: **10.1088/0953-8984/21/6/064215**.

12 T. Zou, X. Xing, Y. Yang, Z. Wang, Z. Wang, R. Zhao, X. Zhang and Y. Wang, Water-soluble ZnO quantum dots modified by (3-aminopropyl) triethoxysilane: The promising fluorescent probe for the selective detection of Cu2+ ion in drinking water, *J. Alloys Compd.*, 2020, **825**, 153904, DOI: **10.1016/j.jallcom.2020.153904**.

13 Z. Yan, Z. Sun, K. Yue, A. Li and L. Qian, CoO/ZnO nanoclusters immobilized on N-doped 3 D reduced graphene oxide for enhancing lithium storage capacity, *J. Alloys Compd.*, 2020, **836**, 155443, DOI: **10.1016/j.jallcom.2020.155443**.

14 S. Anjum, H. Nazli, F. Bashir and K. Mahmood, Structural, Optical and Magnetic Properties of Zn0.5CuxCo0.5-x Dilute Magnetic Semiconductors, *Mater. Today: Proc.*, 2015, **2**, 5552–5558, DOI: **10.1016/j.matpr.2015.11.085**.

15 S. Kammoun and J. El ghoul, Structural and optical investigation of Co-doped ZnO nanoparticles for nanooptoelectronic devices, *J. Mater. Sci.: Mater. Electron.*, 2021, **32**, 7215–7225, DOI: **10.1007/s10854-021-05430-7**.

16 A. Neffati, H. Souissi and S. Kammoun, Electronic structure of Co-doped ZnO nanorods, *J. Appl. Phys.*, 2012, **112**, 083112, DOI: **10.1063/1.4757634**.

17 F. Mselmi, A. Neffati and S. Kammoun, Theoretical investigation of the cathodoluminescence spectra of Co-doped ZnO nanowires, *J. Lumin.*, 2018, **198**, 124–131, DOI: **10.1016/j.jlumin.2018.02.018**.

18 J. El Ghoul and F. F. Al-Harbi, Synthesis, structural, optical and magnetic properties of Gd co-doped ZnO:V nanoparticles, *Solid State Commun.*, 2020, **314–315**, 113916, DOI: 10.1016/j.ssc.2020.113916.

19 N. Patra, S. K. Karuturi, D. Nakamura, M. Higashihata, V. Singh and I. A. Palani, Influence of Ni, Ti and NiTi alloy nanoparticles on hydrothermally grown ZnO nanowires for photoluminescence enhancement, *J. Alloys Compd.*, 2019, **770**, 1119, DOI: 10.1016/j.jallcom.2018.08.160.

20 V. Gandhi, R. Ganesan, H. H. A. Syedahamed and M. Thaiyan, Effect of Cobalt Doping on Structural, Optical, and Magnetic Properties of ZnO Nanoparticles Synthesized by Coprecipitation Method, *J. Phys. Chem. C*, 2014, **118**, 9715–9725, DOI: 10.1021/jp411848t.

21 H. Sarma and K. C. Sarma, X-ray Peak Broadening Analysis of ZnO Nanoparticles Derived by Precipitation method, *International Journal of Scientific and Research Publication*, 2014, **4**). https://citeseerx.ist.psu.edu/viewdoc/download?doi=10.1.1.429.2767&rep=rep1&type=pdf.

22 F. Mselmi, O. Taktak, H. Souissi and S. Kammoun, Correlation between experimental spectroscopic study and crystal-field calculations of Co2+ ions in α-ZnAl2S4 spinel, *J. Lumin.*, 2019, **206**, 319–325, DOI: 10.1016/j.jlumin.2018.10.047.

23 H.-M. Zhang, X. Wan and Z.-M. Zhang, Theoretical studies of the spin Hamiltonian parameters and local structures for the tetragonal Cu2+ and Ni3+ centers in Mg2TiO4, *J. Alloys Compd.*, 2013, **549**, 226–230, DOI: 10.1016/j.jallcom.2012.09.078.

24 H.-M. Zhang, Y.-D. Li, B.-J. Chen, C.-D. Feng and Y.-J. Fu, Theoretical studies on the Spin Hamiltonian parameters and the local structure for Cu2+ in rutile, *J. Alloys Compd.*, 2020, **25**, 154294, DOI: 10.1016/j.jallcom.2020.154294.

25 O. Taktak, H. Souissi and S. Kammoun, Optical absorption properties of ZnF2-RO-TeO2 (R = Pb, Cd and Zn) glasses doped with chromium (III): Neuhauser model and crystal field study, *Opt. Mater.*, 2021, **113**, 110682, DOI: 10.1016/j.optmat.2020.110682.

26 O. Taktak, H. Souissi and S. Kammoun, Optical properties of the phosphors $Zn_2SnO_4:Cr^{3+}$ with near-infrared long-persistence phosphorescence for bio-imaging applications, *J. Lumin.*, 2020, **228**, 117563, DOI: 10.1016/j.jlumin.2020.117563.

27 H. Souissi, O. Taktak and S. Kammoun, Theoretical study by analytical equations of optical properties of the phosphors Zn_2SnO_4 codoped with Cr^{3+} and (Al^{3+} or Eu^{3+}) via the crystal field control, *Opt. Mater.*, 2021, **121**, 111529, DOI: 10.1016/j.optmat.2021.111529.

28 D. J. Newman and B. Ng, *Crystal Field Handbook*, Cambridge University Press, 1st edn, 2000, pp. 28–36.

29 J. S. Griffith, *The Theory of transition-metal ions*, Cambridge university Press, Cambridge, 1961.

30 S. Sugano, Y. Tanabe, H. Kamimura, *Multiplets of Transition-Metal Ions in Crystals*, Academic Press, New York, 1st edn, 1970, pp. 106–111.

31 R. C. Powell, *Physics of Solid-State Laser Materials*, Springer-Verlag, New York, 1998, 1st edn, pp. 215–233.

32 Y. Y. Yeung and C. Rudowicz, Ligand field analysis of the 3d^N ions at orthorhombic or higher symmetry sites, *Comput. Chem.*, 1992, **16**, 207–216, DOI: 10.1016/0097-8485(92)80004-J.

33 C. S. Barret and T. B. Massalski, *Structure of Metals: Crystallographic Methods, Principles and Data*, Pergamon Press, Oxford, 1980.

34 F. C. M. Vande Pol, Thin-film ZnO-properties and applications, *Am. Ceram. Soc. Bull.*, 1990, **69**, 1959–1965. https://jglobal.jst.go.jp/en/detail?JGLOBAL_ID=200902031457640468.

35 G.-L. Tan, D. Tang, D. Dastan, A. Jafari, J. P. B. Silva and X.-T. Yin, Effect of heat treatment on electrical and surface properties of tungsten oxide thin films grown by HFCVD technique, *Mater. Sci. Semicond. Process.*, 2021, **122**, 105506, DOI: 10.1016/j.mssp.2020.105506.

36 A. S. Hassanien, A. A. Akl and A. H. Sáaedicryst, Synthesis, crystallography, microstructure, crystal defects, and morphology of BixZn$_{1−x}$O nanoparticles prepared by sol–gel technique, *CrystEngComm*, 2018, **20**, 1716–1730, DOI: 10.1039/c7ce02173a.

37 M. M. Obeid, H. R. Jappor, K. Al-Marzoki, I. A. Al-Hydary, S. J. Edrees and M. M. Shukur, Unraveling the effect of Gd doping on the structural, optical, and magnetic properties of ZnO based diluted magnetic semiconductor nanorods, *RSC Adv.*, 2019, **9**, 33207–33221, DOI: 10.1039/c9ra04750f.

38 M. P. Dasari, U. Godavarti and V. Mote, Structural, morphological, magnetic and electrical properties of Ni-doped ZnO nanoparticles synthesized by co-precipitation method, *Process. Appl. Ceram.*, 2018, **12**, 100–110, DOI: 10.2298/pac1802100d.

39 R. Mguedla, A. Ben Jazia Kharrat, O. Taktak, H. Souissi, S. Kammoun, K. Khirouni and W. Boujelben, Experimental and Theoretical investigations on optical properties of multiferroic $PrCrO_3$ ortho-chromite compound, *Opt. Mater.*, 2020, **101**, 109742, DOI: 10.1016/j.optmat.2020.109742.

40 K. Joshi, M. Rawat, S. K. Gautam, R. G. Singh, R. C. Ramola and F. Singh, Band gap widening and narrowing in Cu-doped ZnO thin films, *J. Alloys Compd.*, 2016, **680**, 252–258, DOI: 10.1016/j.jallcom.2016.04.093.

41 R. Pappalardo, D. L. Wood and R. C. Linares Jr, Optical Absorption Spectra of Ni-Doped Oxide Systems. I, *J. Chem. Phys.*, 1961, **35**, 1460, DOI: 10.1063/1.1732066.

42 S. Nadupalli, S. Repp, S. Weberb and E. Erdem, About defect phenomena in ZnO nanocrystals, *Nanoscale*, 2021, **13**, 9160–9171, DOI: 10.1039/d1nr00943e.

43 H. Kaftelen, K. Ocakoglu, R. Thomann, S. Tu, S. Weber and E. Erdem, EPR and photoluminescence spectroscopy studies on the defect structure of ZnO nanocrystals, *Phys. Rev. B: Condens. Matter Mater. Phys.*, 2012, **86**, 014113, DOI: 10.1103/physrevb.86.014113.

44 P. Jakes and E. Erdem, Finite size effects in ZnO nanoparticles: An electron paramagnetic resonance (EPR) analysis, *Phys. Status Solidi RRL*, 2011, **5**(2), 56–58, DOI: 10.1002/pssr.201004450.

45 S. Repp, S. Weber and E. Erdem, Defect Evolution of Nonstoichiometric ZnO Quantum Dots, *J. Phys. Chem. C*, 2016, **120**(43), 25124–25130, DOI: **10.1021/acs.jpcc.6b09108**.

46 A. U. Ammar, I. D. Yildirim, F. Bakan and E. Erdem, ZnO and MXenes as electrode materials for supercapacitor devices, Beilstein, *J. Nanotechnol.*, 2021, **12**, 49–57, DOI: **10.3762/bjnano.12.4**.

47 M. H. Aleinawi, A. U. Ammar, M. Buldu-Akturk, N. S. Turhan, S. Nadupalli and E. Erdem, Spectroscopic Probing Of Mn-Doped ZnO Nanowires Synthesized via a Microwave-Assisted Route, *J. Phys. Chem. C*, 2022, **126**(8), 4229–4240, DOI: **10.1021/acs.jpcc.2c00009**.

48 E. Erdem, Microwave power, temperature, atmospheric and light dependence of intrinsic defects in ZnO nanoparticles: A study of electron paramagnetic resonance (EPR) spectroscopy, *J. Alloys Compd.*, 2014, **605**, 34–44, DOI: **10.1016/j.jallcom.2014.03.157**.

49 Y. P. Varshni, Temperature dependence of the energy gap in semiconductors, *Physica*, 1967, **34**, 149–154, DOI: **10.1016/0031-8914(67)90062-6**.

50 F.-Y. Jen, Y.-C. Lu, C.-Y. Chen, H.-C. Wang, C. C. Yang, B.-P. Zhang and Y. Segawa, Temperature-dependent exciton dynamics in a ZnO thin film, *Appl. Phys. Lett.*, 2005, **87**, 252117, DOI: **10.1063/1.2150277**.

51 L. H. Quang, S. J. Chua, K. P. Loh and E. Fitzgerald, The effect of post-annealing treatment on photoluminescence of ZnO nanorods prepared by hydrothermal synthesis, *J. Cryst. Growth*, 2006, **287**, 157–161, DOI: **10.1016/j.jcrysgro.2005.10.060**.

52 G. D. Chen, M. Smith, J. Y. Lin, H. X. Jiang, A. Salvador, N. Sverdlov, A. Botchkarv and H. Morkoc, Photoluminescence studies of band-edge transitions in GaN epitaxial layers grown by plasma-assisted molecular beam epitaxy, *J. Appl. Phys.*, 1996, **79**, 2675H.